# HIGH-RESOLUTION IMAGING OF SOLAR FLARE RIBBONS AND ITS IMPLICATION ON THE THICK-TARGET BEAM MODEL

Säm Krucker[1,2], H. S. Hudson[1,3], N. L. S. Jeffrey[3], M. Battaglia[3], E. P. Kontar[3],
A. O. Benz[2], A. Csillaghy[2], and R. P. Lin[1,4]

[1] Space Sciences Laboratory, University of California, Berkeley, CA 94720-7450, USA; krucker@ssl.berkeley.edu
[2] Institute of 4D Technologies, School of Engineering, University of Applied Sciences Northwestern Switzerland, 5210 Windisch, Switzerland
[3] Department of Physics and Astronomy, University of Glasgow, Glasgow G12 8QQ, UK
[4] Department of Physics, University of California, Berkeley, CA 94720-7300, USA

## ABSTRACT

We report on high-resolution optical and hard X-ray observations of solar flare ribbons seen during the *GOES* X6.5 class white-light flare of 2006 December 6. The data consist of imaging observations at 430 nm (the Fraunhofer *G* band) taken by the *Hinode* Solar Optical Telescope with the hard X-rays observed by the *Reuven Ramaty High Energy Solar Spectroscopic Imager*. The two sets of data show closely similar ribbon structures, strongly suggesting that the flare emissions in white light and in hard X-rays have physically linked emission mechanisms. While the source structure along the ribbons is resolved at both wavelengths (length $\sim 30''$), only the *G*-band observations resolve the width of the ribbon, with values between $\sim 0''.5$ and $\sim 1''.8$. The unresolved hard X-ray observations reveal an even narrower ribbon in hard X-rays (the main footpoint has a width perpendicular to the ribbon of $< 1''.1$ compared to the *G*-band width of $\sim 1''.8$) suggesting that the hard X-ray emission comes from the sharp leading edge of the *G*-band ribbon. Applying the thick-target beam model, the derived energy deposition rate is $> 5 \times 10^{12}$ erg s$^{-1}$ cm$^{-2}$ provided by an electron flux of $1 \times 10^{20}$ electrons s$^{-1}$ cm$^{-2}$ above 18 keV. This requires that the beam density of electrons above 18 keV be at least $1 \times 10^{10}$ cm$^{-3}$. Even if field lines converge toward the chromospheric footpoints, the required beam in the corona has too high a density to be described as a dilute tail population on top of a Maxwellian core. We discuss this issue and others associated with this extreme event, which poses serious questions to the standard thick target beam interpretation of solar flares.

*Key words:* Sun: flares – Sun: X-rays, gamma rays

*Online-only material:* color figures

## 1. INTRODUCTION

Solar flares were discovered by Carrington (1859) and Hodgson (1859) through white-light emissions. Although the emission mechanism of white-light flares is still not understood today, we now know that such radiation is produced at the footpoints of flaring magnetic loops, often also referred to as flare ribbons. Footpoints or ribbons are observed at almost all wavelengths from radio to $\gamma$-rays. Of particular interest to the flare acceleration process are the hard X-ray emissions from the flare ribbons produced by bremsstrahlung of flare-accelerated ($>10$ keV) electrons (e.g., Hoyng et al. 1981; Masuda et al. 2001; Liu et al. 2007). In the current standard flare model, magnetic energy is released in the corona and electrons are accelerated there (see review by Benz 2008). While coronal densities are generally too low to stop energetic electrons, chromospheric densities are high enough. Therefore, the most intense hard X-ray bremsstrahlung sources are at the footpoints of magnetic loops. Coronal hard X-ray sources are significantly fainter, but generally occur at about the same time (see review by Krucker et al. 2008).

To use the hard X-ray observations as a diagnostic tool, the so-called thick-target beam model was developed; this provides simple formulae that allow us to determine the spectrum of the accelerated electrons from their hard X-ray emission (e.g., Brown 1971). In this model, electrons travel from an assumed coronal acceleration site to the footpoints as a dilute beam with the beam density much smaller than the ambient density. The standard model assumes that electrons do not lose

energy in the low-density corona and quickly penetrate to the chromosphere where collision losses dominate and the electrons are thermalized by collision while producing bremsstrahlung emission; the chromosphere is described as a thick-target X-ray source. Applying this model to observations, it was realized immediately that the observed hard X-ray emissions require an efficient conversion of magnetic energy into nonthermal electrons. The acceleration mechanism providing such an efficient conversion is presently not understood.

In this paper, we compare high-resolution ($0''.18$ FWHM) 430 nm (*G*-band) observations from the Solar Optical Telescope (SOT; Tsuneta et al. 2008) on board *Hinode* (Kosugi et al. 2007) with hard X-ray observations from the *Reuven Ramaty High Energy Solar Spectroscopic Imager* (*RHESSI*; Lin et al. 2002). The detailed spectral distribution of white-light flare emission is not well known (e.g., Hudson et al. 2010), but *G*-band images are often used as proxy for the white-light flare emission. Since we are not deriving quantitative estimates involving the spectral shape but only using imaging to describe the source geometry, this simplification does not influence our conclusions. Further SOT *G*-band observations of flares are discussed by Isobe et al. 2007, Wang 2009, and Watanabe et al. 2010. White-light and hard X-ray emissions are known to correlate well, at least for the few events published. These correlations appear in time (e.g., Rust & Hegwer 1975; Hudson et al. 1992; Fletcher et al. 2007), intensity (e.g., Neidig & Kane 1993; Sylwester & Sylwester 2000; Chen & Ding 2005; Watanabe et al. 2010), and space (e.g., Xu et al. 2004, 2006). While energetic protons have also been suggested as the energy source for white-light emission
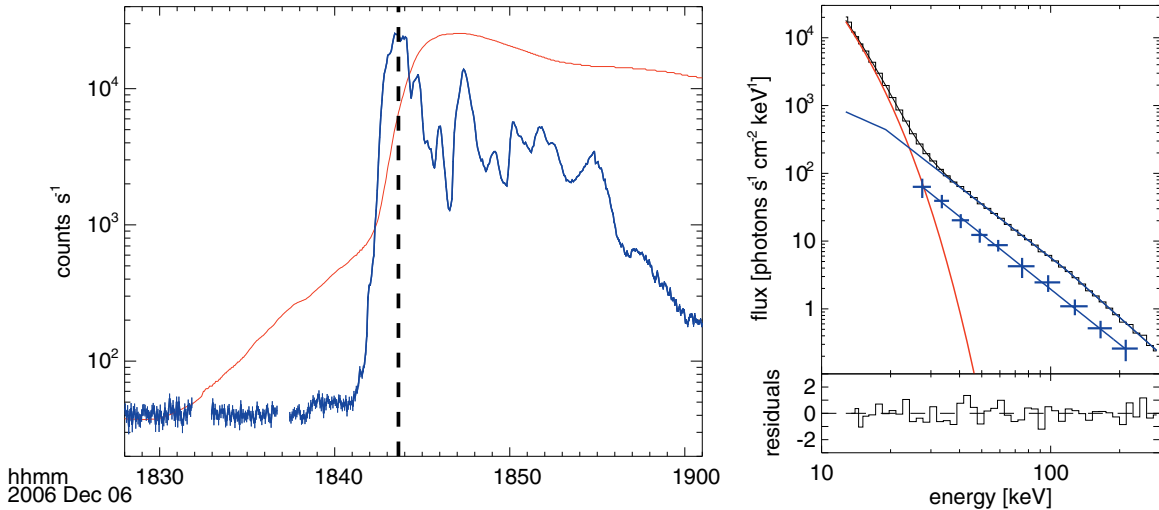
**Figure 1.** Left: *GOES* soft X-ray (red) and *RHESSI* 25–100 keV hard X-ray (blue) time profile of the *GOES* X6.5 flare from 2006 December 6. The time of the *G*-band image shown in Figure 2 is given by the dashed vertical line. Right: flare-integrated photon spectrum observed by detector 4 at the time of the *G*-band image integrated over 8 s. The red and blue curves are a thermal fit and a broken power-law fit to the data (black). The blue points with error bars give the spectrum of the main footpoint with a power-law fit.

(A color version of this figure is available in the online journal.)

(e.g., Najita & Orrall 1970; Simnett 1986), the tight correlation with hard X-ray emission favors the electrons that produce the hard X-rays as the source of energy for the white-light emission.

The study presented here is the most detailed spatial comparison reported so far. The event discussed (X6.5, S06E63, SOL2006-12-06T18:47) ranks among the *RHESSI* flares with the best counting statistics in the non-thermal range, providing a unique opportunity for a spatial comparison. In the second part of the paper, we use the derived parameters, in particular the footpoint area and the energy deposition rate, to test the standard flare scenario whereby electron beams accelerated in the corona produce the hard X-ray emissions.

## 2. OBSERVATIONS AND DATA ANALYSIS

The *Hinode*/SOT observations provide *G*-band (430.5 nm, $\Delta\lambda = 0.8$ nm) images at a spatial resolution of $0''.18$ FWHM (Wedemeyer-Böhm 2008). Since the Sun is bright at this wavelength, very short exposure times are sufficient (0.03 s for the images taken during this flare). The cadence of *G*-band SOT images is generally low compared to the time variability of the hard X-ray flux, which shows time variations for most flares significantly shorter than 1 minute. For the 2006 December 6 event, only a 2 minute SOT image cadence is available. However, one image was taken just at the time of the main hard X-ray peak (18:43:38.5 UT; Figure 1). Our analysis will focus on this moment.

The *G*-band image at the hard X-ray peak time (Figure 2) shows two resolved flare ribbons that are elongated ($\sim30''$ for the southern ribbon, $\sim12''$ for the northern ribbon), but rather narrow (with a thickness between $\sim0''.5$ and $\sim1''.8$ FWHM). The same ribbons are also seen in the *Transition Region and Coronal Explorer* (*TRACE*) 1600 Å image (at a spatial resolution of $\sim1''$) taken at almost the same time (18:43:39.0 UT). The response of this *TRACE* 1600 Å filter is broad (for further discussion see Fletcher et al. 2007) making its interpretation in general more difficult. The good spatial agreement with the *G*-band source structure suggests that the 1600 Å emissions show the short-wavelength end of the white-light continuum, but there are

also 1600 Å sources (see Figure 3, center panel, around [−844, −116]) without a *G*-band counterpart, possibly reflecting the broad spectral response of the *TRACE* 1600 Å filter.

### 2.1. Hard X-Ray Imaging

Results of *RHESSI* imaging and time variations of this flare have already been published by Kaufmann et al. (2009) in the context of its THz emission (see review by Krucker et al. 2011). Here we concentrate on the analysis of hard X-ray images in the non-thermal energy range (25–100 keV) using CLEAN (Hurford et al. 2002) around the time of the *G*-band image (18:43:38.5 UT). We use the CLEAN algorithm because it is the most straightforward and best understood of the *RHESSI* imaging algorithms. Neither MEM nor PIXON algorithms are considered here because of their tendency to break up unresolved sources and in some cases demonstrate a not-well-understood tendency toward super-resolution. Forward-fit algorithms are not available for a complex source structure such as that seen in this flare. For a detailed comparison of *RHESSI* imaging techniques, we refer to Dennis & Pernak (2009). The CLEAN images shown in Figure 2 were reconstructed including the finest sub-collimator (i.e., at highest spatial resolution) giving a point-spread function (PSF; Hurford et al. 2002) of the CLEAN image of $3''.0$ FWHM. These images apply "uniform weighting" of the different sub-collimators. As *RHESSI* imaging cannot match the integration time of SOT, we compare *RHESSI* images integrated over 4, 8, and 16 s (i.e., at multiples of the *RHESSI* spin period) around the time of the SOT image. Since the duration of the main hard X-ray burst is longer (about 84 s FWHM, see Figure 1) than the selected integration times, the different integration times may not significantly affect the image comparison. While a 4 s integration time provides a rather noisy image with a dynamic range of $\sim3$ (i.e., contours below 30% in Figure 2(d) show noise), the 8 s integration provides an improved image with a dynamic range of $\sim5$, a typical value for *RHESSI* images. Longer time integrations show the same source structure, but only minimally improve the image quality (Figure 2(f)). For the analysis presented below, we therefore use the image integrated over 8 s. Footpoint
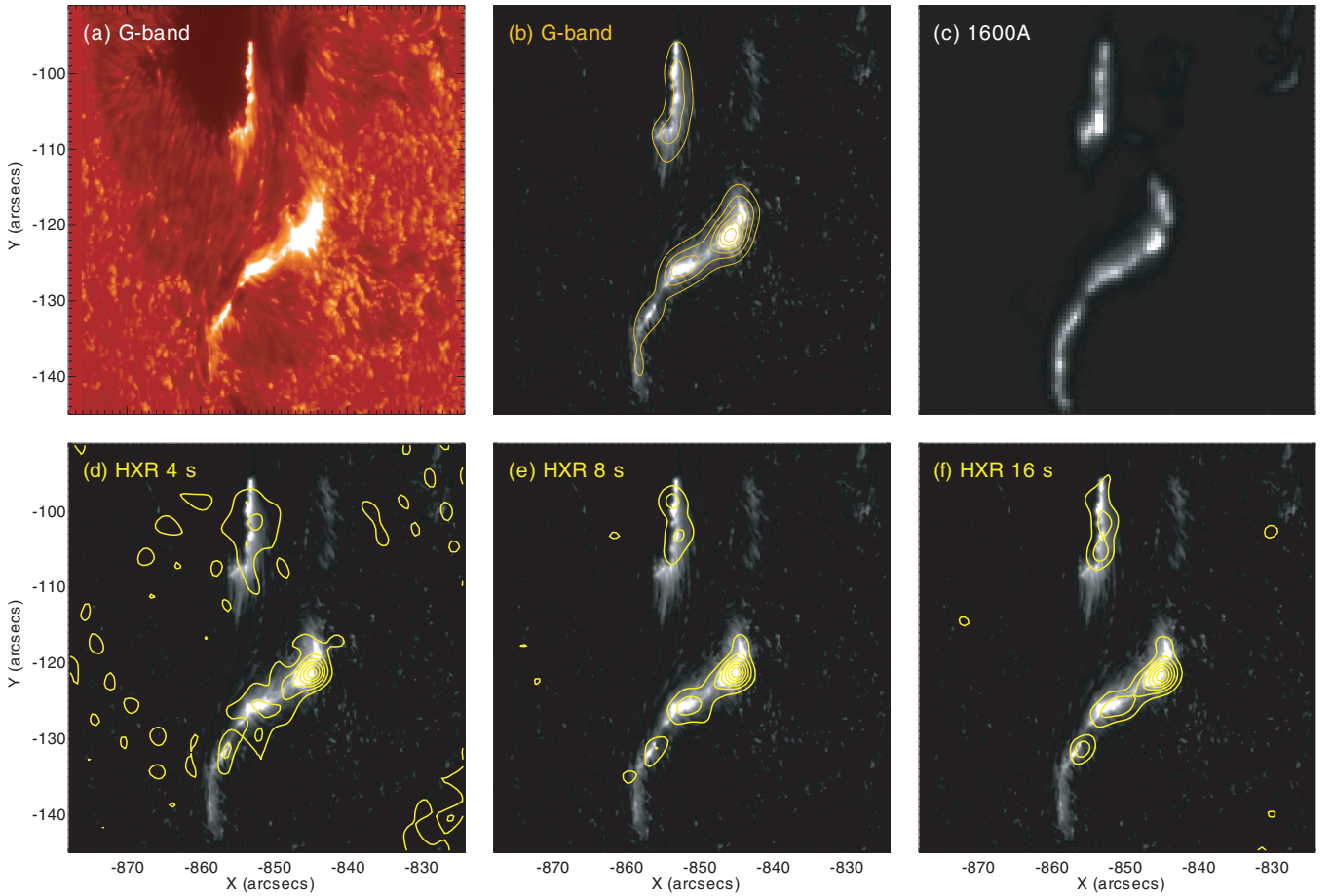
**Figure 2.** Imaging results in *G* band, UV, and 25–100 keV hard X-rays. (a) *G*-band image during hard X-ray peak (18:43:38.5 UT). (b) Same image with the pre-flare image taken at 18:39:39 UT subtracted. The dark yellow contours show the same image convolved with the *RHESSI* PSF (3″.0 FWHM). (c) *TRACE* 1600 Å image taken at 18:43:39 UT. ((d)–(f)) *RHESSI* CLEAN contours (3″.0 FWHM resolution) in the energy range 25–100 keV at 4, 8, and 16 s time integration, respectively. The shown image is the same *G*-band image as shown in panel (b). All contour plots (Figures 2 and 3) use the same contours levels (15%, 30%, 45%, 60%, 75%, 90% of the peak flux).

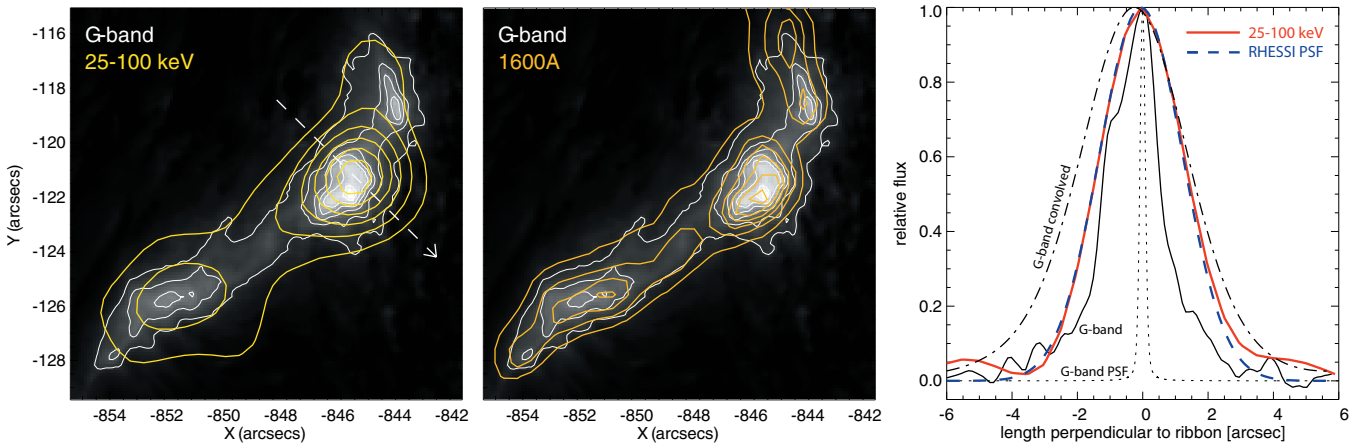(A color version of this figure is available in the online journal.)



**Figure 3.** Details of the southern footpoint. Left: the image shows the background-subtracted *G*-band emission with 25–100 keV hard X-ray contours from the 8 s integrated data plotted in yellow (same contours as in Figure 2). The thin white contours are the *G*-band emission (same contours as used for the hard X-ray data). (center) The same *G*-band image is shown with *TRACE* 1600 Å contours using again the same contour levels. Right: spatial profiles perpendicular to the ribbon of the brightest footpoint (the white dashed arrow in the figure to the left gives the direction of the shown profiles). The black curves show the *G*-band profile (solid, ~1″.8 FWHM), the *G*-band PSF (dotted, ~0″.18 FWHM from Wedemeyer-Böhm 2008), and the *G*-band profile convolved with the *RHESSI* PSF (dash-dotted, ~3″.8 FWHM). The observed hard X-ray profile is given in red (~3″.0 FWHM) and the *RHESSI* PSF is the blue dashed curve (3″.0 FWHM). Since the absolute pointing of the *G*-band image is not well known, the relative position of the shown *G* band and hard X-ray profiles are not known accurately enough for a sub-arcsecond comparison.

(A color version of this figure is available in the online journal.)

motions, as often observed in flares (e.g., Qiu et al. 2002), can smear out source shapes if integrated over a long time period. Maximal observed velocities of footpoint motions are up to 100 km s$^{-1}$ and more typically 10 km s$^{-1}$ (e.g., Yang et al. 2009). Hence, for an 8 s integration time, footpoint motion could smear out the flare ribbons by up to ~1″. Since the observed hard X-ray sources look similar for all integration times (Figure 2), footpoint motions do not appear to contribute much to the observed source shape, either perpendicular to or along the ribbons. This is somewhat surprising, as times with intense hard X-ray fluxes such as seen in the 2006 December 6 flare tend to show fast footpoint motions (e.g., Krucker et al. 2003, 2005). However, projection effects due to the flare location close to the east limb could at least partially hide any footpoint motions.

The ribbons seen in the *G* band and in hard X-rays are similar not only spatially, but also in relative intensity. For a more detailed comparison, we convolved the *G*-band image with a PSF of the CLEAN image (3″0 FWHM). Figure 2(b) shows the original *G*-band image with the convolved image as contours using the same levels as the *RHESSI* images. Within the available dynamic range, the correlation between the hard X-ray and *G*-band ribbons is excellent. The cross-correlation of the convolved *G*-band and hard X-ray images is used for co-alignment of the images shown in Figure 2. The only missing part in our observations is the absolute and relative altitudes (heights in the solar atmosphere) of the *G*-band and hard X-ray sources to sub-arcsecond accuracies; otherwise the *G*-band and hard X-ray sources appear to be cospatial.

### 2.2. Detailed Analysis of the Brightest Footpoint

In the following, we discuss in detail the size of the brightest hard X-ray footpoint on the southern ribbon. Figure 3 shows the hard X-ray profile of the brightest footpoint normal to the ribbon. The profile has the same width as the PSF function, indicating that the hard X-ray emission normal to the ribbon is unresolved at 3″0. A different way of checking if a source is unresolved is using relative amplitudes (e.g., Schmahl & Hurford 2003). As expected for unresolved sources, the relative amplitudes perpendicular to the ribbon for sub-collimators 1 and 3 are found to be the same. Unresolved ribbon structures in perpendicular directions are also reported by Dennis & Pernak (2009) for several *RHESSI* flares. As the observed source size in a CLEANed image, $S_o$, is a convolution of the actual source size, $d$, with the size of the PSF, $S_{psf}$, the unresolved observations indicate that width of the hard X-ray ribbon is smaller than $S_{psf} \sim 3″0$. Assuming Gaussian source shapes, the actual source size becomes $d = (S_o^2 - S_{psf}^2)^{0.5}$. The main footpoint has nearly the same size as the PSF to within an error estimate of 0″2. Thus the actual size must be less than $d < (3.2^2 - 3.0^2)^{0.5} = 1″1$.

The *G*-band image taken at much higher resolution (0″18 FWHM) shows a perpendicular extent of 1″8 (FWHM). Hence, the *G*-band ribbon is wider than the hard X-ray ribbon. This can also be seen in the *G*-band profile convolved with the *RHESSI* PSF (Figure 3, right); this has a FWHM of 3″8, significantly larger than the observed hard X-ray source at ~3″0. The *G*-band emission clearly shows an asymmetric spatial profile with the inner part of the ribbon being much broader than the outer part (Isobe et al. 2007 used the expression "sharp leading edge"). Masuda et al. (2001) had suggested the presence of such perpendicular structure, but with observations of significantly lower resolution. Additional to the main peak, there is at least one minor *G*-band source on the shoulder of the main source (Figure 3, right, at ~1″). As this minor

source is located at the inner side of the ribbon, it could be *G*-band emissions from a previously flaring ribbon element that is decaying (Neidig et al. 1993; Hudson et al. 2006; Qiu et al. 2010). This additional source is not expected to be seen in hard X-rays as the hard X-ray emissions stop abruptly when flare-accelerated electrons disappear. White-light emissions on the other hand are expected to have a decay time independent of the acceleration process. Using just the sharp leading edge to determine an FWHM size of the main *G*-band source, we get a size of ~1″1. This is just at the upper end of the hard X-ray source size derived above.

To derive the actual area of the main footpoint we have to take projection effects into account. The orientation of southern flare ribbon is mostly in the radial direction (the ribbon is aligned ~20° away from radial). Projection effects therefore mostly influence the ribbon length, with the ribbon width not affected within the uncertainties of the upper limit mentioned above.

To assess the projection effects we make three estimates with differing assumed radial dimensions: flat (no thickness), 1″, and 2″ (cases 0, 1, and 2, respectively). The observed length of the main footpoint in the radial direction is 3″4 FWHM (see Figure 4, bottom panel) giving a deconvolved size of 1″6. For a hard X-ray source with no vertical extent (flat source, case 0), the correction for the viewing angle gives a length of 3″2. For vertically extended sources with $h_1 = 1″$ and $h_2 = 2″$ (cases 1 and 2), we get slightly lower values of 2″6 and 2″1, respectively. Since the ribbon is slightly rotated relative to the radial direction, the actual length $l$ of the hard X-ray source along the ribbon is slightly longer. For cases 0, 1, and 2, we get $l_0 = 3″4$, $l_1 = 2″8$, and $l_2 = 2″2$, respectively.

Combined with the upper limit of the width of the hard X-ray source and the different assumption on the vertical extent we get footpoint areas of $A_0 < 2.0 \times 10^{16}$ cm$^2$, $A_1 < 1.6 \times 10^{16}$ cm$^2$, $A_2 < 1.3 \times 10^{16}$ cm$^2$, respectively, and an upper-limit volume of the hard X-ray source between $1.2 \times 10^{24}$ cm$^3$ and $1.9 \times 10^{24}$ cm$^3$.

### 2.3. Compton Backscattering

The above size estimates do not account for the apparent size increase produced by Compton backscattering from the photosphere (e.g., Schmahl & Hurford 2002; Kontar et al. 2006; Battaglia et al. 2011). Hence, the actual source size could be even smaller than the upper limit derived above. To investigate this, we apply the albedo simulations of Kontar & Jeffrey (2010) for the parameters of the main hard X-ray footpoint, using the energy range 25–50 keV. For the vertical extent of the footpoint source, simulations for two different geometries are performed: a flat source at an altitude of 1″4 above the photosphere and a vertically extended source of height 1″ from 0″4 to 1″4 above the photosphere. Figure 4 shows the simulated source profiles in radial (left and center) and horizontal (right) directions, parameterized for beam anisotropy via an up/down ratio (see Kontar & Jeffrey 2010 for details). Since the southern flare ribbon is roughly aligned with the radial direction, simulations in radial and horizontal directions are relevant for the length and width of footpoint area, respectively.

Since our flare occurred near the limb, the profiles in the radial direction show the effect of albedo more clearly than in horizontal direction. For a flat footpoint (Figure 4, left), albedo radiation produces a double source, but for the case with finite vertical extent, the albedo contribution is smeared out, thus resulting in an asymmetric profile (Figure 4, center). However, since *RHESSI* cannot spatially resolve the two peaks,
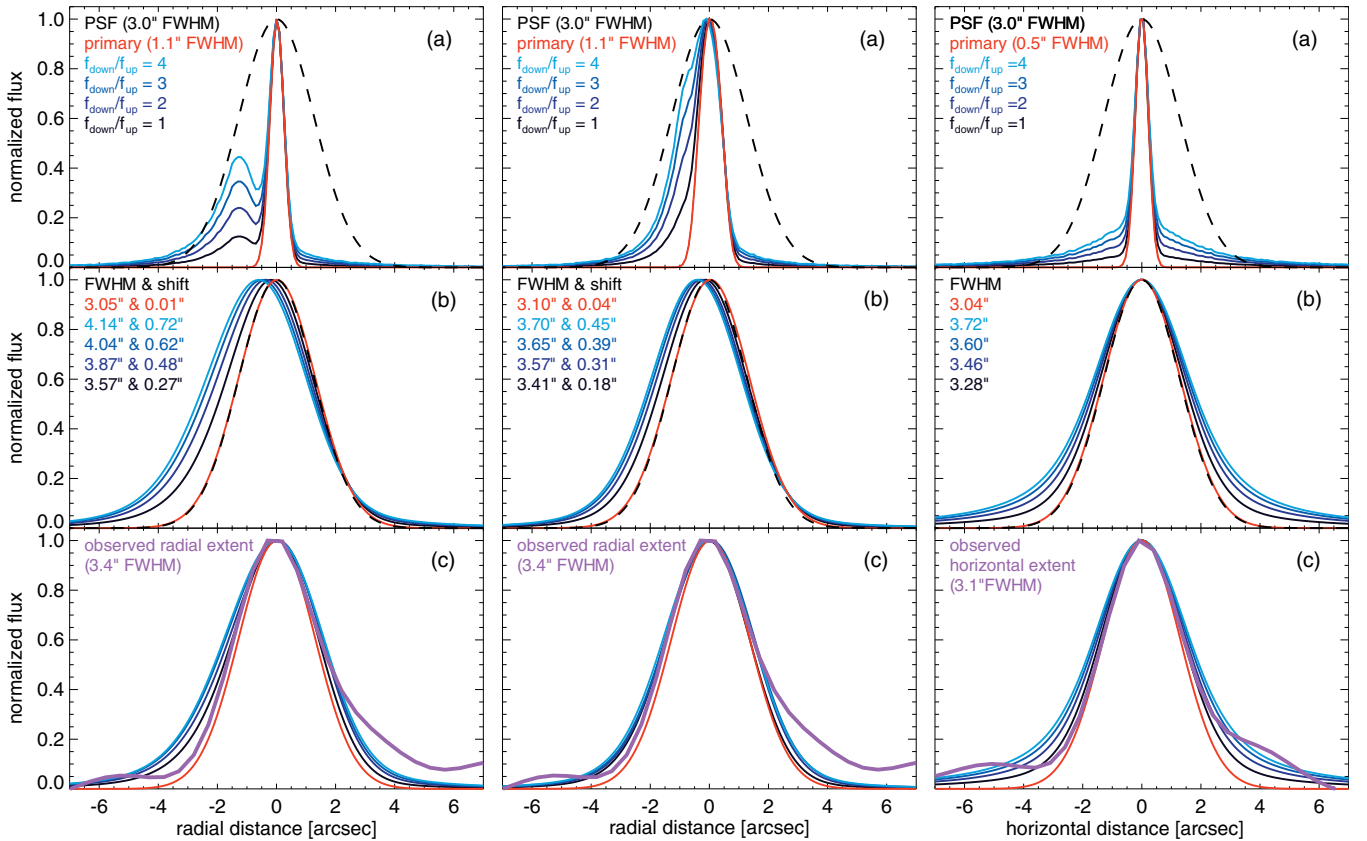
**Figure 4.** Monte Carlo simulations of the effect of Compton backscattering (albedo) in the energy range from 25 to 50 keV on the apparent sources size using the method described in Kontar & Jeffrey 2010. The shown profiles in radial (left and center) and horizontal (right) direction are for the parameter of the peak time of the 2006 December 6 flare: flare location at 850″ from solar center and spectral photon index of 2.3. Two geometries for the vertical distribution of the source are considered: a flat source at an altitude of 1″.4 above the photosphere (left) and an extended source from 0″.4 to 1″.4 above the photosphere (center and right). For each simulation, the following panels are shown: (a) simulated profiles of the total emission (primary and albedo) for different anisotropy values are given in blue. For comparison, the primary source and the PSF is given in red and black (dashed), respectively. (b) Same profiles convolved with the *RHESSI* PSF. The values of the FWHM and the shift given in the top left corner are derived by fitting a Gaussian to the convolved profiles. (c) The observed radial and horizontal profiles through the main hard X-ray source are given in magenta (note that the horizontal profile is taken in a slightly different directions than the one shown in Figure 3). For an easier comparison, the shown convolved profiles are shifted in radial direction so that all profiles peak at zero. The radial simulations are shown for both models of vertical extent (left and center) for a primary source size of 1″.1. Since the horizontal profiles for both models look qualitatively very similar, only the simulation for the extended source is shown for a primary of 0″.5.

(A color version of this figure is available in the online journal.)

both simulations predict that *RHESSI* should see similar source shapes in the radial direction with an increased source size and a shift in position (see Kontar & Jeffrey 2010, Battaglia et al. 2011 for further discussion). For large anisotropies (the simulations assume a range of down/up ratios for the photon fluxes), the increase in the observed source size could be up to 1″. However, spectral and multi-spacecraft observations (of different flares) favor the isotropic case (e.g., Kane et al. 1998; Kontar & Brown 2006), making the size increase rather small and therefore difficult to observe with *RHESSI*.

In the horizontal direction, the albedo radiation adds symmetric wings to the primary source (Figure 4, right). Since *RHESSI* does not resolve the primary source, the simulated *RHESSI* profiles are broadened when compared to the primary. For a source of 1″.1, even the isotropic case gives an increase in size to 3″.44. Since the observed size is smaller (Section 2.2), this suggests that the primary source could be smaller than 1″.1. The simulation for a primary source of 0″.5 gives a size of 3″.28 (see Figure 4, right). This is still larger than the observed size, but likely within the combined uncertainties of the observations and simulations.

In summary, the simulations show that the spatially unresolved flare ribbon reported in this paper does not contradict

the source size broadening expected from albedo. The observational limitations together with the unknown source altitude and the unknown degree of anisotropy, however, do not allow us to extract further information on the actual source size. In any case, albedo can only increase the source size, and the upper limits derived above are therefore valid independent of the albedo effect.

### 2.4. Spectral Analysis

To estimate the energy deposition rate, the spectrum at peak time is discussed in the following. The spectral analysis of front-segment data reported here are done using standard *RHESSI* analysis techniques correcting for pulse pile-up and albedo. Since the statistics for this event are excellent, the spectral fits are preformed for each detector separately. We use the four detectors with the best spectral response (detectors 1, 4, 8, and 9). Background subtraction is not an issue for the energies considered here for such a bright flare. Fits with a thermal component and a double broken power-law work well (Figure 1, right) and give closely similar results for the different detectors with $\chi^2$ between 0.7 and 1.4. In the following, we give averaged values of the fit parameters obtained from the

different detectors using the standard deviation of the parameters as rough error estimates. The thermal fit gives a temperature of $37.4 \pm 0.4$ MK and an emission measure (EM) of $(1.1 \pm 0.1) \times 10^{49}$ cm$^{-3}$. The non-thermal fit reveals a slope of $\gamma_1 = 2.64 \pm 0.04$ up to a break energy of $124 \pm 15$ keV and a slightly steeper spectrum at higher energies ($\gamma_2 = 2.96 \pm 0.05$). As typically for solar flare spectral fitting, the low energy cutoff energy, $E_0$, cannot be fitted accurately because the steep thermal spectrum and only an upper limit of $E_0 = 18 \pm 3$ keV can be derived. The normalizations of the different detectors give consistent results within 10% with fluxes at 50 keV of $33 \pm 3$ photons s$^{-1}$ cm$^{-2}$ keV$^{-1}$. Compared to statistical studies (e.g., Alaoui et al. 2011), these fit parameters are typical for very energetic flares. Using the thick target formula (e.g., Brown 1971), the derived spectral parameters give an energy deposition rate of $2.4 \times 10^{29} (E_0/18 \text{ keV})^{-1.6}$ erg s$^{-1}$. The largest uncertainty is introduced by the poorly constrained low-energy cutoff. A statistical study of *RHESSI* flares (Kontar et al. 2008a) showed that for all events in their sample thermal emission is hiding the low energy cutoff indicating that the low-energy cutoff should be below 12 keV. Hence, the upper limit $E_0$ used here is a typical value.

To derive the spectrum of the main hard X-ray footpoint, we apply standard *RHESSI* imaging spectroscopy techniques using CLEANed images (e.g., Krucker & Lin 2002). The spectrum of the main footpoint (Figure 1, right) is found to have a shape similar to that of the flare-integrated spectrum, but with about one-third of the total flux. The reduced statistics especially at high energies makes it impossible to detect the break around $\sim$120 keV. A power-law fit gives a spectral slope of $\gamma = 2.6 \pm 0.2$ and fluxes at 50 keV of $12 \pm 2$ photons s$^{-1}$ cm$^{-2}$ keV$^{-1}$, and the energy deposition rate within the main hard X-ray footpoint becomes $0.8 \times 10^{29} [E_0/18 \text{ keV}]^{-1.6}$ erg s$^{-1}$.

## 3. DISCUSSION

The *Hinode* and *RHESSI* observations of the X-class flare on 2006 December 6 reveal that the white-light and hard X-ray emissions originate from extended flare ribbons with similar source shapes and relative intensities. The altitude above the photosphere of the two emissions, however, cannot be determined. Nevertheless this close association, in combination with earlier findings, strongly suggests that flare-accelerated electrons are somehow involved in the production of white-light flares. Since ion precipitation is observed to occur spatially separated from electron precipitation at least in some flares (Hurford et al. 2003, 2006), the association between white-light emissions and hard X-rays does not favor the idea that flare-accelerated energetic ($\simeq$30 MeV) ion beams produce the white-light emission. If electrons are indeed involved in production of the white-light emission, it is unclear how the hard X-ray ribbons that are generally supposed to originate in the chromosphere (e.g., Kontar et al. 2008b; Saint-Hilaire et al. 2010) are related to the white-light sources that would naively be expected to lie in the photosphere. However, no simultaneous observations are currently available showing the absolute positions at both wavelengths. Future observations should focus on the three-dimensional structure of the sources.

### 3.1. Energy Deposition Rate per Area in the Thick-target Approximation

In the following, the derived upper limit of the main footpoint area and the standard thick-target beam formula (e.g., Brown

1971) are used to estimate a lower limit of the energy deposition rate per area. The calculations are done for the brightest footpoints only to get the maximal heating rate. For the area, we use the upper limit $A_1$ giving an energy deposition rate of $>5 \times 10^{12} [A/A_1]^{-1} [E_0/18 \text{ keV}]^{-1.6}$ erg s$^{-1}$ cm$^{-2}$ provided by $1 \times 10^{20}$ electrons s$^{-1}$ cm$^{-2}$ above 18 keV. While the different estimates of the footpoint area only slightly change the energy deposition rate, the largest uncertainty comes from the poorly constrained cutoff energy. For $E_0 = 12$ keV (e.g., Kontar et al. 2008a) give $>1 \times 10^{13}$ erg s$^{-1}$ cm$^{-2}$, while a large cutoff values of 50 keV gives $>1 \times 10^{12}$ erg s$^{-1}$ cm$^{-2}$. Further uncertainties are introduced by the several assumptions in the standard thick-target analysis; for example, the standard formula takes the stopping column density to be fully ionized. If this is not the case, the energy deposition can be lower; for an un-ionized target, the heating rate is $\sim$3 times smaller (e.g., Holman et al. 2011). Nevertheless, the derived value is a very large lower limit, at least several times larger than the solar luminosity per unit area $\mathcal{L}_\odot \sim 7 \times 10^{10}$ erg s$^{-1}$ cm$^{-2}$ that peaks at optical wavelengths. This indicates that there is enough energy in non-thermal electrons to locally produce a white-light signature above the white-light emission level (e.g., Watanabe et al. 2010). The heating rate within the hard X-ray source can be calculated using the thick-target approximation and the estimated source volume giving $7 \times 10^4 [E_0/18 \text{ keV}]^{-1.6}$ erg s$^{-1}$ cm$^{-3}$ or a heating rate per ambient electron of $4.3 [n/10^{13} \text{ cm}^{-3}]^{-1} [E_0/18 \text{ keV}]^{-1.6}$ keV s$^{-1}$. The response of the plasma within the hard X-ray footpoint to this energy input is currently not understood. Radiation hydrodynamic simulations of electron precipitation in flares (e.g., Abbett & Hawley 1999) have not yet successfully dealt with this large an intensity; Allred et al. (2005) were able to calculate only 16 s of evolution for their F11 model, roughly at $\mathcal{L}_\odot$. Future simulations should focus on extending the parameter space to investigate the effects of such large heating rates.

To better understand the number of precipitating electrons per area, we compare it to the number of thermal electrons in the volume defined by the stopping column density. For a cutoff energy of 18 keV, we estimate $5 \times 10^{19}$ thermal electrons cm$^{-2}$ within this stopping column (e.g., Brown 1971). Using the mean energy of the radiating electrons of $\sim$29 keV increases the number by about a factor of two. Even in the latter case, within a second, the number of precipitating electrons will exceed the total number of electrons initially contained by this column. In the absence of any loss mechanism that takes energy away from the particles in this column on this timescale, the energy deposition within it must energize all ambient electrons energies comparable to those of the assumed electron beam. Hence, within a fraction of the hard X-ray burst duration, the precipitation of electrons must drastically change the nature of the medium. This simple consideration shows that the idea of a stopping column density of cold plasma is only adequate to describe this event for a short time interval at the onset of the hard X-ray burst. Hence, a modified or even different scenario should be explored.

A slightly different way of quantifying the number of precipitation electrons is by estimating a density of accelerated electrons within the hard X-ray producing region. Assuming that electrons travel in a straight line with the velocity corresponding to their mean energy ($\sim$29 keV), using the electron precipitation rate from above, a beam density of $1 \times 10^{10}$ cm$^{-3}$ for electrons above 18 keV is derived. The absence of direct measurements of the ambient density in the corona and the effect of field

convergence limits a detailed comparison of the derived beam density with the ambient coronal density. A rough upper limit for the ambient coronal density can be derived from the absence of non-thermal hard X-ray emission from the corona, requiring a coronal column density below $5 \times 10^{19}$ electrons cm$^{-2}$. From the footpoint separation we estimate a half loop length of $2 \times 10^9$ cm$^{-2}$ and the upper limit of the coronal density is of the order of a few time $10^{10}$ cm$^{-3}$. Hence, even if field lines converge toward the hard X-ray footpoint sources (e.g., Kontar et al. 2010), the beam densities in the corona would still be a significant fraction of the ambient density. Modern interpretations of the radio observations (White et al. 2011) tend to confirm the view that the radiating electrons cannot be regarded as a dilute beam. Such intense beams were not envisioned in the simple thick-target beam model, which implicitly assumes the beam to be dilute (i.e., beam density $\ll$ ambient density). The dynamics of such intense beams and their return currents (e.g., Lee et al. 2008) should be further studied to investigate if such intense beams can be physically possible.

### 3.2. Instantaneous Density of Accelerated Electrons within the Hard X-Ray Footpoint Source

A further estimate we wish to highlight is the density of accelerated electrons within the hard X-ray source. Independent of how the flare-accelerated electrons are transported (as a beam or locally accelerated), the instantaneous number of hard X-ray producing electrons, $N_{inst}$, can be derived if the ambient density $n$ within the hard X-ray source is known (e.g., Brown 1971; Lin 1974). Since we do not have a measurement for $n$ for our event, we adopt a typical value of $10^{13}$ cm$^{-3}$ (e.g., Saint-Hilaire et al. 2010). To derive the instantaneous number density, $n_{inst}$, we assume a hard X-ray source thickness $h_1 = 1''$ and use the area $A_1$. For the main footpoint at the hard X-ray peak time we then get an instantaneous density of accelerated electrons above $E_c = 18$ keV of $n_{inst} = 2 \times 10^9 [n/10^{13}$ cm$^{-3}]^{-1}$ cm$^{-3}$ (e.g., Lin 1974), and $n_{inst}/n = 2 \times 10^{-4} [n/10^{13}$ cm$^{-3}]^{-2}$. This estimate highlights again the large densities of non-thermal electrons required, as discussed above. However, the instantaneous population of accelerated electrons in the hard X-ray producing region can be described as a tail population, at least for high enough ambient densities. For typical ambient densities between $10^{13}$ cm$^{-3}$ and $10^{14}$ cm$^{-3}$ (e.g., Kontar et al. 2008b), the accelerated electrons are a fraction between $10^{-4}$ and $10^{-6}$ of the ambient density.

### 4. CONCLUSIONS

The parameters derived from the high-resolution imaging observations presented in this paper show that the intensity of energy deposition for the event discussed is higher than for previously reported events and may still underestimate the actual intensity. These observations provide stringent tests to the present-day standard flare model of electron beams as the main transport mechanism of energy from the coronal acceleration site to the footpoints. While radio observations (e.g., Bastian et al. 1998) and in situ electron observations (e.g., Lin 1985) clearly establish that electron beams are created during solar flares, we do not know yet if very bright hard X-ray footpoints such as presented in this paper can be produced by analogous beams penetrating the lower atmosphere.

## REFERENCES

Abbett, W. P., & Hawley, S. L. 1999, ApJ, 521, 906
Alaoui, M., Krucker, S., Saint-Hilaire, P., & Lin, R. P. 2011, ApJ, submitted
Allred, J. C., Hawley, S. L., Abbett, W. P., & Carlsson, M. 2005, ApJ, 630, 573
Bastian, T. S., Benz, A. O., & Gary, D. E. 1998, ARA&A, 36, 131
Battaglia, M., Kontar, E. P., & Hannah, I. G. 2011, A&A, 526, A3
Benz, A. O. 2008, Living Rev. Sol. Phys., 5, 1
Brown, J. C. 1971, Sol. Phys., 18, 489
Carrington, R. C. 1859, MNRAS, 20, 13
Chen, Q. R., & Ding, M. D. 2005, ApJ, 618, 537
Dennis, B. R., & Pernak, R. L. 2009, ApJ, 698, 2131
Fletcher, L., Hannah, I. G., Hudson, H. S., & Metcalf, T. R. 2007, ApJ, 656, 1187
Hodgson, R. 1859, MNRAS, 20, 15
Holman, G., Aschwanden, M. J., Aurass, H., et al. 2011, Space Sci. Rev.
Hoyng, P., Duijveman, A., Machado, M. E., et al. 1981, ApJ, 246, L155
Hudson, H. S., Acton, L. W., Hirayama, T., & Uchida, Y. 1992, PASJ, 44, L77
Hudson, H. S., Fletcher, L., & Krucker, S. 2010, Mem. Soc. Astron. Ital., 81, 637
Hudson, H. S., Wolfson, C. J., & Metcalf, T. R. 2006, Sol. Phys., 234, 79
Hurford, G. J., Krucker, S., Lin, R. P., et al. 2006, ApJ, 644, L93
Hurford, G. J., Schmahl, E. J., Schwartz, R. A., et al. 2002, Sol. Phys., 210, 61
Hurford, G. J., Schwartz, R. A., Krucker, S., et al. 2003, ApJ, 595, L77
Isobe, H., Kubo, M., Minoshima, T., et al. 2007, PASJ, 59, 807
Kane, S. R., Hurley, K., McTiernan, J. M., et al. 1998, ApJ, 500, 1003
Kaufmann, P., Trottet, G., Giménez de Castro, C. G., et al. 2009, Sol. Phys., 255, 131
Kontar, E. P., & Brown, J. C. 2006, ApJ, 653, L149
Kontar, E. P., Dickson, E., & Kašparová, J. 2008a, Sol. Phys., 252, 139
Kontar, E. P., Hannah, I. G., Jeffrey, N. L. S., & Battaglia, M. 2010, ApJ, 717, 250
Kontar, E. P., Hannah, I. G., & MacKinnon, A. L. 2008b, A&A, 489, L57
Kontar, E. P., & Jeffrey, N. L. S. 2010, A&A, 513, L2
Kontar, E. P., MacKinnon, A. L., Schwartz, R. A., & Brown, J. C. 2006, A&A, 446, 1157
Kosugi, T., Matsuzaki, K., Sakao, T., et al. 2007, Sol. Phys., 243, 3
Krucker, S., Bastia, T. S., Gimenez, C. G., et al. 2011, A&AR, submitted
Krucker, S., Battaglia, M., Cargill, P. J., et al. 2008, A&AR, 16, 155
Krucker, S., Fivian, M. D., & Lin, R. P. 2005, Adv. Space Res., 35, 1707
Krucker, S., Hurford, G. J., & Lin, R. P. 2003, ApJ, 595, L103
Krucker, S., & Lin, R. P. 2002, Sol. Phys., 210, 229
Lee, K. W., Büchner, J., & Elkina, N. 2008, A&A, 478, 889
Lin, R. P. 1974, Space Sci. Rev., 16, 189
Lin, R. P. 1985, Sol. Phys., 100, 537
Lin, R. P., Dennis, B. R., Hurford, G. J., et al. 2002, Sol. Phys., 210, 3
Liu, C., Lee, J., Gary, D. E., & Wang, H. 2007, ApJ, 658, L127
Masuda, S., Kosugi, T., & Hudson, H. S. 2001, Sol. Phys., 204, 55
Najita, K., & Orrall, F. Q. 1970, Sol. Phys., 15, 176
Neidig, D. F., & Kane, S. R. 1993, Sol. Phys., 143, 201
Neidig, D. F., Kiplinger, A. L., Cohl, H. S., & Wiborg, P. H. 1993, ApJ, 406, 306
Qiu, J., Lee, J., Gary, D. E., & Wang, H. 2002, ApJ, 565, 1335
Qiu, J., Liu, W., Hill, N., & Kazachenko, M. 2010, ApJ, 725, 319
Rust, D. M., & Hegwer, F. 1975, Sol. Phys., 40, 141
Saint-Hilaire, P., Krucker, S., & Lin, R. P. 2010, ApJ, 721, 1933
Schmahl, E. J., & Hurford, G. J. 2002, Sol. Phys., 210, 273
Schmahl, E. J., & Hurford, G. J. 2003, Adv. Space Res., 32, 2477
Simnett, G. M. 1986, Sol. Phys., 106, 165
Sylwester, B., & Sylwester, J. 2000, Sol. Phys., 194, 305
Tsuneta, S., Ichimoto, K., Katsukawa, Y., et al. 2008, Sol. Phys., 249, 167
Wang, H.-M. 2009, Res. Astron. Astrophys., 9, 127
Watanabe, K., Krucker, S., Hudson, H., et al. 2010, ApJ, 715, 651
Wedemeyer-Böhm, S. 2008, A&A, 487, 399
White, S. M., Benz, A. O., Chrite, S., et al. 2011, Space Sci. Rev.
Yang, Y.-H., Cheng, C. Z., Krucker, S., Lin, R. P., & Ip, W. H. 2009, ApJ, 693, 132
Xu, Y., Cao, W., Liu, C., et al. 2004, ApJ, 607, L131
Xu, Y., Cao, W., Liu, C., et al. 2006, ApJ, 641, 1210